Microscopic correlation of doping distribution and luminescence in a nitride laser junction by Photonic Atom Probe

Eric Weikum,[1] Abraham Diaz-Damian,[1,†] Jonathan Houard,[1] Gérald Da Costa,[1] Fabien Delaroche,[1] Angela Vella,[1] Grzegorz Muzioł,[2,†] Henryk Turski,[2] and Lorenzo Rigutti[1,*]

[1]*Groupe de Physique des Matériaux, CNRS, University of Rouen Normandie, 76000 Rouen, France*

[2]*Institute of High Pressure Physics of the Polish Academy of Sciences "UNIPRESS", 01–142 Warszawa, Poland*

(Received 17 April 2024; accepted 28 June 2024; published 18 July 2024)

The Photonic Atom Probe is applied to the study of nanoscale field-emission tip specimens containing a section of III-N device constituted by a sequence of alloyed and doped sections. Different sections produce specific but spectrally overlapping luminescence signals. The possibility of collecting photoluminescence spectra during the field evaporation of the specimen allows for disentangling different doping-related luminescence lines and to correlate the different spectral contributions to the specific properties of the doping distributions. In particular, the spectral components of the luminescence related to Mg impurities at energies between 3.0 eV and 3.3 eV have been investigated, and correlated with the Mg concentration and 3D distribution in different sections of the device.

DOI: 10.1103/PhysRevMaterials.8.074603

I. INTRODUCTION

The attribution of optical emissions with specific properties (signatures) to structural or chemical features of a nanoscale system can be considered as a relevant problem in correlative microscopy applied to photonics and optoelectronics. Nowadays there are multiple approaches allowing for such correlations: cathodoluminescence (CL) inside a scanning transmission electron microscope (STEM) is an example [1]; CL implemented as a 3D mapping technique in a FIB/SEM tomography approach [2] scanning tunneling luminescence (i.e., electroluminescence induced by a scanning tunneling microscope tip through current injection) is another [3]. On the other hand, absorption properties can be addressed by TEM-based techniques such as electron energy loss spectroscopy (EELS) [4]. The recently developed photonic atom probe (PAP) couples the capabilities of atom probe tomography (APT) and photoluminescence (PL) spectroscopy in an *in situ*, online configuration, and is capable of distinguishing optical signatures of different quantum wells lying at distances of around 10 nm and with peak wavelengths differing by several nm [5]. In the PAP, a set of PL spectra is collected while the specimen is being field evaporated as in a standard APT experiment. The set of PL spectra may be extremely rich of information but its interpretation is not always straightforward, as all spectra are issued by the remaining volume of the specimen at a given evaporation stage. Also, the spatial resolution for the optical spectroscopy is one dimensional, as PL spectra only vary as a function of the progress of the evaporation front [5,6]. However, the PAP may be advantageous to apply with respect to other microscopic hyperspectral techniques such as SEM-CL or TEM-CL because it is the only correlative microscopy technique yielding, so far, the possibility of correlating the optical properties of a nanoscale system with a 3D map of atomic positions. Such a map, indeed, carries information about alloy fractions, doping concentration, local order, interface definition, and presence of chemically identifiable defects.

The PAP has so far been employed in the study of III-N and II-O quantum confining heterostructures only—although it has also demonstrated to be able to collect signals from disordered alloys such as (Mg,Zn)O. It has not yet been applied to the study of point-defect emission, which could significantly extend its domain of interest. In particular, PAP can target the problem of identifying and localizing the doping impurities responsible for optical emission, as we demonstrate here for a III-N heterostructure device.

Typically, III-N heterostructures are grown epitaxially using either metal-organic vapor phase epitaxy (MOVPE) [7] or molecular beam epitaxy (MBE). Most crystal growth methods unintentionally introduce light element impurities (C, O), leading to *n*-type conductivity in epitaxially grown III-nitrides [8]. Si serves as a substitutional dopant on the Ga site for *n*-type doping, resulting in a shallow donor state [9]. Alternatively, Ge doping has shown promising properties, achieving high charge carrier concentrations [10,11]. Ge doping allows for higher doping levels compared to Si doping and introduces less lattice strain [12,13]. The choice of Ge as a dopant is an interesting option in tunnel junctions (TJs), in order to ensure the presence of the high concentration of free electrons necessary to create the both a degenerate *n*-type layer and a strong field gradient [13,14]. Understanding these dynamics is crucial for optimizing light-emitting diode (LED) or laser diode (LD) performance and emission characteristics. Such correlation between electrical device properties and device

*Contact author: lorenzo.rigutti@univ-rouen.fr

†Present address: LATMOS, Université Versailles Saint-Quentin 11, 78280 Guyancourt, France.

TABLE I. Details of the analyzed device structure including alloy fractions and doping concentrations as assessed by PAP.

Layer #	Matrix	III-site fraction (SIMS)	III-site fraction (APT)	Doping impurity	Doping concentration [cm^{-3}] (SIMS)	Doping concentration [cm^{-3}] (APT)	Thickness (PAMBE +XRD) [nm]	Note
15	GaN			Si	10^{19}		50	
14	AlGaN	$X_{Al} = 0.034$	$X_{Al} = 0.04$	Si	8×10^{18}		550	Device cladding
13	GaN			Si	10^{18}		150	LD *n*-type side
12	InGaN	$X_{In} = 0.072$	$X_{In} = 0.08$				60	LD barrier
11	InGaN	$X_{In} = 0.22$	$X_{In} = 0.22$				11	LD active region
10	InGaN	$X_{In} = 0.064$	$X_{In} = 0.08$				80	LD barrier
9	GaN						25	Unintentionally doped
8	GaN			Mg	10^{19}	8.1×10^{18}	20	LD *p*-type side
7	GaN			Mg	3.5×10^{18}	5.3×10^{18}	350	Transition region
6	GaN			Mg	1.2×10^{19}	9.2×10^{18}	250	Transition region
5	InGaN	gradient	$X_{In} = 0.09$	Mg	gradient	gradient	22	TJ upper cladding
4	InGaN	$X_{In} = 0.21$	$X_{In} = 0.15$	Mg	10^{20}	1.1×10^{20}	5	TJ *p*-type
3	InGaN	$X_{In} = 0.21$	$X_{In} = 0.15$	Ge	5×10^{20}	1.2×10^{20}	5	TJ *n*-type
2	InGaN	gradient	$X_{In} = 0.09$	Si	3×10^{19}		25	TJ lower cladding
1	GaN			Si	3×10^{19}		150	
0	GaN							Substrate

structure has already been quite thoroughly elucidated by the combined application of APT and electron holography on a TJ/LED in which the LED structure and the TJ *p*-type side were grown by MOVPE, while the Ge-doped *n*-type side of the TJ were grown by MBE [14]. The APT study showed that Mg segregates at the TJ interface, and diffuses into the Ge-doped layer—a major deviation from the expectations based on the growth parameters. Electron holography reveals a TJ depletion width of ∼7 nm, in agreement with band diagram simulations based on the dopant distribution extracted by APT, sufficient to ensure the correct operation of the device.

Concerning *p*-type doping of GaN, crucial for LED and LD development, it is typically based on Mg [15]. Plasma-assisted MBE (PAMBE) facilitates the growth of high-quality GaN/AlGaN/InGaN heterostructures at lower temperatures than MOVPE [16]. *p*-type conductivity can be achieved without the need of post-growth thermal activation and without transferring the sample between reactors [17]. That is why, using PAMBE, comparison between structures with the TJ grown before and after the active region can be conducted [18]. Two GaN-based LEDs with opposite *p*- and *n*-doping orders produced by PAMBE exhibit different electroluminescence properties due to polarization-induced changes in band structure [19]. Most interestingly for our study, PAMBE is a lower-temperature growth, which is expected to avoid the Mg clustering typically observed for MOVPE-grown *p*-type GaN [20–22], a phenomenon, which depends on doping concentration and growth temperature, and which is also related to the formation of structural defects in the form of pyramidal inversion domains [20,23].

Beyond electrical properties, *p*-type doping in GaN may act as a radiative recombination center through acceptor-to-band or donor-acceptor pair transitions (DAP). This latter mechanism is particularly important in III-N materials, where intrinsic defects act as donor centers. Mg-related luminescence has been thoroughly studied during around three decades [24–29]. Such luminescence is usually studied in homogeneous thin films, where it is not susceptible to overlap with heterostructure-related emissions.

In this paper, we show that PAP can resolve the optical signatures of strongly overlapping doping-related PL emissions within a complex and relatively thick device structure, namely a III-nitride double junction containing multiple layers of different alloy composition and doping, including a TJ. Beyond that, the optical signatures can be directly related to the 3D distribution of the chemical species within the sample, which represents a complementary capability with respect to other nanoscale spectral imaging techniques such as cathodoluminescence.

II. EXPERIMENTAL SECTION

A. Analyzed sample

The general structure of the sample is reported in detail in Table I. The entire structure is grown in a single-growth run, under the metal-rich conditions typically used by PAMBE, on a commercially available Ga-polar GaN substrate. More details on the used growth conditions can be found in [19]. Growth starts with an *n*-type conductive layer that serves as a basis on which the TJ is deposited. The information about the composition of different layers is obtained via SIMS both for the alloying content (in the following referred to as III-site fraction)—the profiles of the III-site fractions of Al and In are reported in Fig. 1(a), as well as the concentration of (Mg, Si, Ge) dopants [Fig. 1(b)]. The TJ itself (layers 2 to 5, Table I) consists of the highly doped and higher In content central region (layers 3 and 4) and two surrounding layers (layers 2 and 5) with lower In content. The core of the TJ consists of two highly doped layers. The *n*-type TJ layer is doped with Ge, the upper *p*-type layer with Mg. The highly *p*-doped layer of the has a Mg concentration $n_{Mg} = 3 \times 10^{20}$ cm^{-3} . A Mg-doped section (layers 6 to 8) connects the TJ to the LD junction. Here, the doping was introduced in order to ensure a good flow of electrical current between the two junctions. The

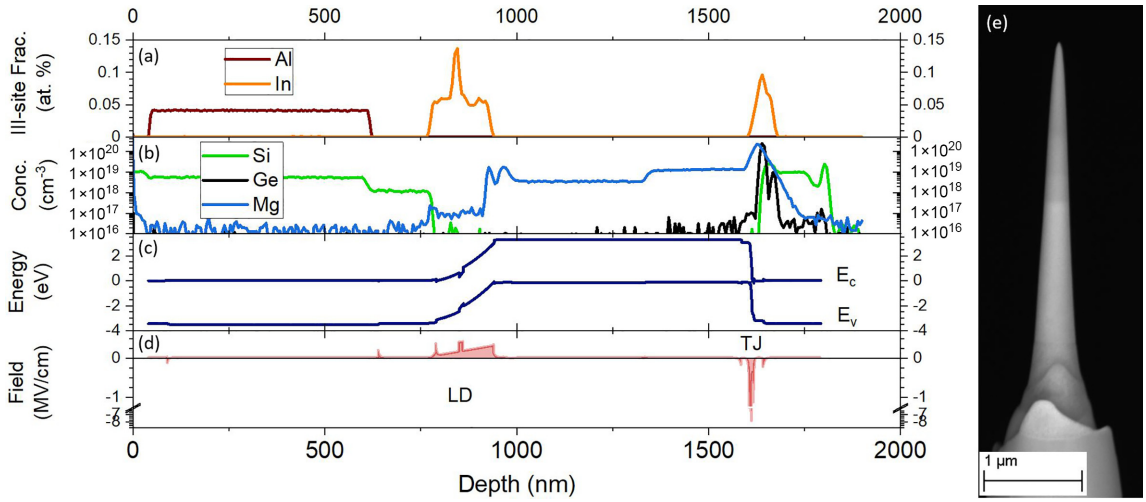

FIG. 1. (a) SIMS profile of the III-site fraction of Al and In. (b) SIMS profile of the concentration of Si (green), Ge (black), and Mg (blue) doping. (c) Band diagram simulated based on the nominal layer thicknesses, III-site fractions and doping concentrations, (d) corresponding field distribution along the structure. (e) Field emission tip containing the whole device structure, as prepared by FIB and ready for PAP analysis.

doping concentration in these layers represents a compromise between the conductivity of the *p*-doped layers and the optical losses due to absorption on Mg [30]. The LD region (layers 10 to 12) is separated from this *p*-type region by the thin unintentionally doped GaN layer 9. The active region of the LD is composed of a 11-nm-thick quantum well ($x_{In} \sim 0.22$). which is surrounded by a lower and upper waveguide layer with $x_{In} \sim 0.06$, which provide sufficient optical mode confinement. Subsequently, a GaN:Si layer precedes an AlGaN:Si cladding, with $x_{Al} \sim 0.04$ (layers 13 and 14, respectively).

The SIMS profile and the nominal composition/thickness parameters do not significantly differ. Based on this information, a device band diagram can be straightforwardly calculated using one-dimensional Poisson, drift-diffusion, and Schrodinger solver 1D-DDCC [31]. For the purpose of the presented calculations, default set of material parameters and activation energies of 10 meV [11] and 190 meV [32], independent of dopant concentrations, for *n*- and *p*-types, respectively, were used [Fig. 1(c)]. The most significant conclusions about the simulated band structure is that the junction fields have absolute values around 0.5 MV/cm within the LD junction and up to 8 MV/cm at the TJ itself. An electric field is present in all InGaN sections of the device, as visible in Fig. 1(d).

The sample is prepared for APT analysis according to a standard protocol based on the use of focused ion beam (FIB), as described elsewhere [5]. One of the four needle-shaped specimens prepared for this study and analyzed within the PAP is shown in Fig. 1(e) and embeds the whole device structure.

B. Photonic Atom Probe experiment

The technical details of the instrument used in this study are discussed in Ref. [6]. The nanometric needle-shaped specimen is polarized with a voltage $V_{DC} = 4-8$ kV, leading to an apex electric field of a few tens of V/nm [33,34]. Field ion evaporation is triggered by femtosecond laser pulses at the repetition rate of 400 kHz. The specimen temperature is set to T = 80 K. The specimen is illuminated by a laser spot with size estimated as slightly larger than two microns (i.e., it illuminates the whole evaporated section of the specimen, without the need of repositioning during the experiment) and an average power of 10 µW. The spot size is limited by the imperfections of optical elements and is larger than the diffraction limit $w \approx \lambda/(2NA) = 443$ nm, where $\lambda = 266$ nm the laser wavelength and NA = 0.3 is the numerical aperture of the focusing optics. PL spectra were acquired with a 600/mm grating in a 320-mm focal length spectrometer, with a spectral resolution of around 0.3 nm. The CCD array integration time for each acquisition was set to 90 s. The evaporated ions are detected by a time resolved and position sensitive detector [35], which records the impact position of ions and their time of flight for standard APT analysis. Each PL spectrum collected during the evaporation and APT analysis is stored in a matrix of spectra and is labeled by with an integer index i_{PL}, referred to as the "spectrum index". This is also stored in the APT data file as an attribute of each ion detected during the collection of the corresponding PL spectrum. The analysis of mass spectra, along with the discussion on the compositional accuracy of our measurements, is reported in detail in the Supplemental Material (SM) [36] (including Ref. [37]). The 3D reconstruction [Fig. 2(a)] was obtained by the application of a reconstruction algorithm based on the evolution of the applied voltage [38]. The following set of parameters was used: apex field = 21.8 V/nm, projection point $m + 1 = 1.65$, curvature factor = 1.25, and reconstruction detection efficiency $\eta_{rec} = 0.35$. Notice that this reconstruction is obtained for an extremely long sample with a single set of parameters, adjusted in order to match the evaporated length of the specimen. For this reason, slight deviations from planarity can occur at heterointerfaces—a reconstruction artefact that does not impact the major conclusions of this paper. Remarkably, the resulting reconstructed lengths of the InGaN sections corresponding to the LD and to the TJ are well reproducing the nominal ones, while the relatively low

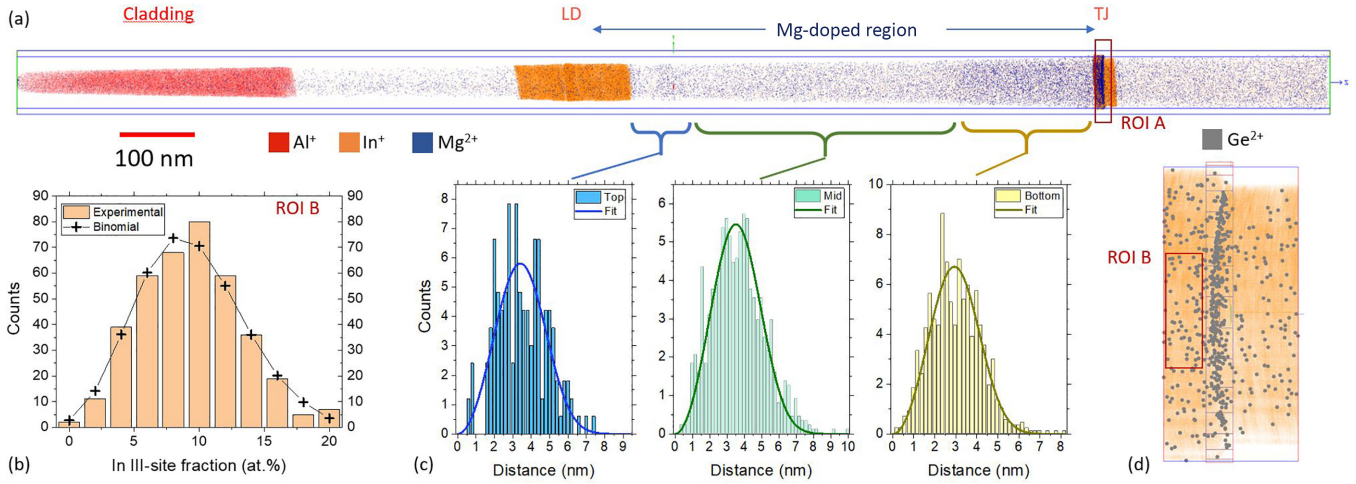

FIG. 2. Relevant data issued from the APT analysis. (a) Reconstructed volume of the whole device structure. The analyzed thickness spans over around 1.5 μm. (b) Frequency distribution analysis of the In distribution in an InGaN section of the tunnel junction [ROI B, see (d)], showing random In distribution. (c) First-nearest-neighbor analysis of the Mg doping in three regions of the *p*-type section, each doped with a different Mg concentration. The experimental histograms are well fitted by the random distribution expected for each doping concentration, showing absence of clustering for Mg. (d) Zoom of the reconstructed region of the tunnel junction (ROI A) showing in grey the distribution of the Ge dopants.

value of η_{rec} is quite common in the APT analysis of III-N structures [39].

III. RESULTS

A. Atom Probe data

The reconstructed volume of one of the four analyzed specimens (the one yielding the best quality of PL and APT) is displayed in Fig. 2(a), while a 5-nm-thick slice of the reconstructed volume is shown in Fig. 3(a). Only a subset of ion species is shown for clarity, i.e., Al (red), In (orange), Mg (blue), and Ge (grey). Notice that APT has no access to Si doping, as Si-related peaks are hidden by N_2^+, N^+, and possible N_xH^{n+} peaks [40]. The reconstructed volume clearly shows—from left to right—part of the AlGaN cladding layer, the LD junction and the TJ region. Mg doping is distinguishable in the region between the two InGaN heterojunctions. Notice that the blue dots outside of this region correspond to noise, as it can be demonstrated by local mass spectrum analysis.

The III-site fraction profile of In is reported in Fig. 3(b) as a function of the evaporated depth coordinate d. The profile clearly visualizes the presence of the LD and TJ regions. Frequency distribution analysis has been performed on all different InGaN sections. An example of III-site In fraction statistical distribution, extracted from the ROI B (a subvolume of layer 5), is shown in Fig. 2(b). The analysis for layer 5 yields an average fraction $x_{In} = 0.090 \pm 0.006$, with a chi-square parameter $\chi^2 = 13.1$ over $N_{dof} = 10$ degrees of freedom, which turns into a p value $p = 0.3$, consistent with a random distribution. Similar results hold for all InGaN layers and can be compared with the SIMS results as reported in Table I.

The distribution of Mg was analyzed by first-nearest-neighbor (1NN) statistical analysis. The distributions of the Mg 1NN distances are displayed in Fig. 2(c) for three different regions, namely layers 6, 7, and 8 (from right to left). All distributions indicate that Mg is in solid solution, without the formation of any cluster. Notice that this holds for high Mg concentrations as in layers 6 and 8 ($n_{Mg} > 10^{19}$ cm^{-3}), for which clustering usually occurs in MOVPE-grown GaN:Mg [21,41,42]. Notice that Mg is also present at the core of the TJ itself, and that it exhibits a tail within the *n*-doped part of the TJ, consistently with previous analyses performed on MOVPE-MBE grown structures [14]. The Mg concentration profile, reported in Fig. 3(b) also allows establishing that the noise level is of the order of 3×10^{18} cm^{-3}, corresponding to the mass spectrum baseline in the neighborhood of the Mg^{2+} mass peaks. The absolute error on the concentration measurement is therefore quite high for all analyzed layers, i.e., $\Delta n_{Mg} = 10^{18}$ cm^{-3}.

Ge doping is localized in layer 3, as displayed in Fig. 2(d). The quantification of Ge was complicated by the fact that Ge peaks overlap with the thermal tails of the Ga peaks (see the SM for details [36]). As already mentioned, the slight curvature of the interfaces in the APT reconstruction is an artifact of the reconstruction algorithm and does not have a major influence on the conclusions of this paper. The Ge atoms are considered to be present in a section of the specimen, which has the thickness (t = 5 nm), which is expected for the Ge-rich section of the TJ. The Ge dopant concentration estimated here is $n_{Ge} = 1.2 \pm 0.8 \times 10^{20}$ cm^{-3}. In order to verify if some Ge might have left the center of the TJ, the local mass spectra of the adjacent InGaN layers are investigated. No $^{74}Ge^+$ or a $^{74}Ge^{2+}$ peaks are observed in these zones. The concentration of doping impurities (except for Si) compares fairly well with the SIMS results (Table I).

B. Photoluminescence spectra

The sequence of subbandgap PL spectra collected during the evaporation of the field-emission needle specimen is

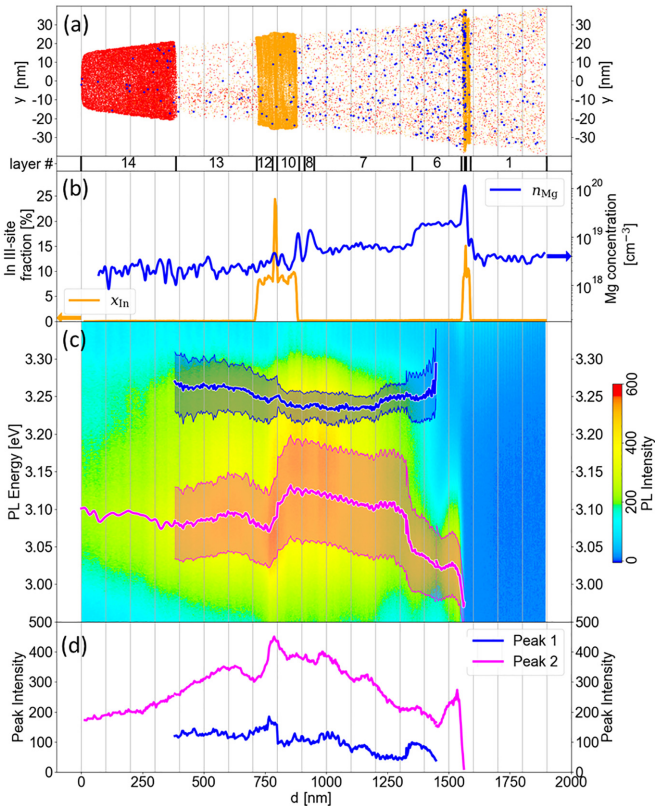

FIG. 3. Correlated PAP data as a function of the reconstructed depth coordinate d. (a) A 5-nm-thick slice of the reconstructed volume, displaying Al (red), In (orange), and Mg (blue) atom positions. Notice that the spatial coordinate x scale is expanded for clarity and the layer number is reported at the bottom of the graph. (b) Composition profiles displaying the In III-site fraction (orange, left-hand ordinates) and the Mg concentration (blue curve, right-hand ordinates). (c) Sequence of PL spectra. The peak energies $E_{PL,m}(i_{PL})$ of sub-bandgap Peaks 1 (pink) and 2 (blue), along with the width of the spectral component $\sigma_{m,i_{PL}}$ have been superimposed to the color plot. (d) Evolution of the intensities $I_m(i_{PL})$ of Peak 1 (pink) and Peak 2 (blue). An animated version of (a) and (c) is available in the SM [36].

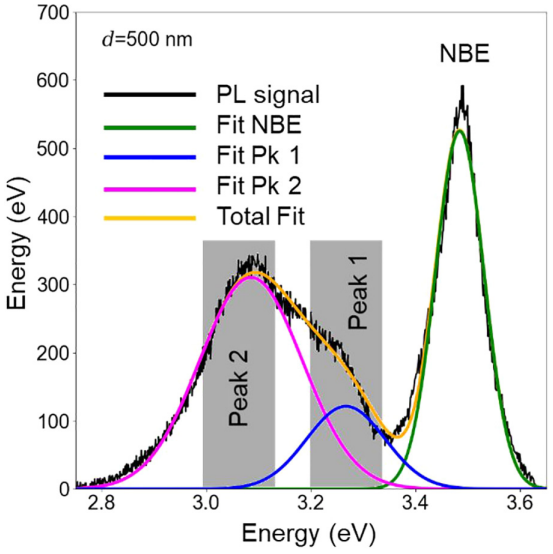

FIG. 4. PL spectrum indexed by $i_{PL} = 75$, corresponding to the depth coordinate of the reconstructed volume $d = 500$ mn (layer 13). The graph also traces the gaussian functions used for the fit, along with the spectral interval in which the investigated contributions of Peak 1 (3.19–3.3 eV) and Peak 2 (2.98–3.17 eV) are located.

reported in Fig. 3(c), while two examples of full recorded PL spectra are reported in Fig. 4 for clarity. The abscissa in Fig. 3(c) corresponds to the average reconstructed depth d of all ions detected during the acquisition of the spectrum indexed by a given i_{PL}. The PL spectra consist of three main spectral components: two sub-bandgap peaks, labeled as Peak 1(peak energy in the interval 3.19–3.3 eV) and Peak 2 (peak energy in the interval 2.98–3.16 eV), as shown in Fig. 4. A GaN near-band-edge emission was also recorded. This emission has been considered for accurate peak analysis, but is not reported in Fig. 3(c). Figure 4 also displays examples of the fitting functions used to extract the peak intensity $I_m(i_{PL})$, the energy $E_{PL,m}(i_{PL})$, and the spectral width $\sigma_m(i_{PL})$ of each component m of the spectrum and for each i_{PL} index. The energy and the peak width of Peaks 1 and 2 are superimposed to the set of PL spectra in Fig. 3(c), while their intensities are traced in Fig. 3(c). These are Gaussian functions that, despite not being the most adapted to accurately replicate the exact shape of the spectral components, have the advantage of being described by a restricted set of parameters. More details about the fitting procedure are given in the SM [36].

IV. DISCUSSION

Based on the complete dataset issued from the PAP experiment, a correlation between the APT and the PL data can be carried out. Nevertheless, some caveats are necessary. One should indeed keep in mind that (i) the PL signal indexed by the integer i_{PL} is emitted by the entire nonevaporated volume of the tip illuminated by the laser beam [5] (this effect could, in principle, be reduced by coating the specimen with a metal [43] or a compound [44] having a low skin depth for PL excitation, but this approach has not been tested in practice yet); (ii) the intensity of a localized emitter is first enhanced as it gets closer to the evaporating apex surface, then decreases and obviously vanishes when it is evaporated [45]; and (iii) finally, a light emitter may undergo spectral shifts induced by the mechanical action (tensile stress) of the electric field present at the apex surface [46]. The effect of the electric field, in particular, depends partly on the geometry of the field emitter and the evaporation progression, partly on the presence of layers with different evaporation field. The first mechanism is such that stress in any tip position typically increases and evolves from uniaxial to hydrostatic as the evaporation front gets closer. Concerning the second mechanism, the electric field is expected to increase when InGaN or AlGaN layers are evaporated in a structure such as the device under investigation [39]. These effects may allow measuring the strain state induced by the field during an APT experiment, but will not be quantitatively addressed in this paper, which primarily targets the attribution of spectral signatures.

A. Evolution of PL spectra

The sub-bandgap PL contributions continuously evolve in intensity, width and peak energy during the measurement [Figs. 3(c) and 3(d)].

(i) *Peak 1*. Peak 1 becomes distinguishable after the evaporation of the AlGaN upper cladding layer. Reliable fits can be performed only starting from $d = 400$ nm. It undergoes a slight red shift and a slight intensity decrease when the evaporation front crosses the QW, then it remains quite stable in energy and intensity until the approach of the highly doped GaN:Mg layer 6. Here, it blue shifts and—most importantly—vanishes *gradually before* the evaporation front has reached the TJ, and before the Peak 2. Notice that the Peak 1 quite significantly overlaps with the Peak 2, the latter having a larger width. Interestingly, Peak 1 blue shifts while vanishing—a behavior opposite to that of Peak 2.

(ii) *Peak 2*. Peak 2 is visible from the beginning of the experiment to the evaporation of layer 5. As the evaporation front approaches the LD junction, it slightly red shifts, then increases its intensity during the evaporation of the QW, then gradually blue shifts and decreases in intensity during the evaporation of the LD lower cladding layer. At the beginning of the evaporation of the GaN:Mg section, it reaches its maximum energy, i.e., $E_{PL2,\max} = 3.14$ eV. It then gradually red shifts as the *p*-type moderately doped GaN:Mg layer 7 is evaporated. It suddenly red shifts again and decreases in intensity when the evaporation front enters the highly-doped GaN:Mg layer 6. Finally, it red shifts again to the final energy $E_{PL2,\min} = 2.98$ eV and bleaches when the TJ is evaporated. We notice that the final bleaching of this spectral component is nonmonotonous—a fact for which we did not find a nonambiguous explanation, but which may be related to the charge carrier dynamics when the TJ field becomes close to the evaporation front. The key features about this peak are the following: (i) it undergoes a strong intensity decrease upon the evaporation of the LD section and (ii) it vanishes *swiftly* as the evaporation of the TJ upper cladding begins.

B. Correlation between below-bandgap PL signatures and 3D reconstruction

The evolution of the two Peaks 1 and 2 can be interpreted through and correlated with the 3D reconstruction issued from the APT analysis. The attributions of the two peaks can be justified as follows:

(i) Peak 1 can be interpreted as related to vertical DAP PL emission, also referred to as UVL (UV-luminescence) line in the literature on doped GaN [29]. Peak 1 strongly dims and disappears when layer 6 is being evaporated and its energy corresponds well to previous literature data [24,25,27,42,47,48]. This is also reported in Fig. 5(b), where the PL energies of the peak are plotted as a function of the Mg concentration. Two data points issued from the PAP are reported. The first corresponds to the beginning of the evaporation of layer 7, which is moderately doped with Mg ($n_{Mg} = 5.3 \times 10^{18}$ cm^{-3}), while the second corresponds to the vanishing peak recorded during the evaporation of layer 6 (which is relatively highly doped, $n_{Mg} = 9.2 \times 10^{18}$ cm^{-3}). Although it can be expected that the first data point is actually the result of the emission of layer 7 (layer 6 is still present, but it lies deeper, further from the apex) and that the second one from layer 6 only; care should be taken before establishing trends of the emission energy as a function of the Mg concentration as it can be done for the literature datasets reported in Fig. 5, selected among the references on DAP in GaN:Mg as those that report the DAP PL energy as a function of the Mg concentration explicitly. Some care should also be taken upon this comparison, as the cited references mostly relate to MOVPE-grown material, where a large portion of the Mg forms pyramidal inversion domains [23,49] and appears as clustered in the APT reconstructions [50]. In any case, the quantitative agreement between the present data and the literature is satisfying.

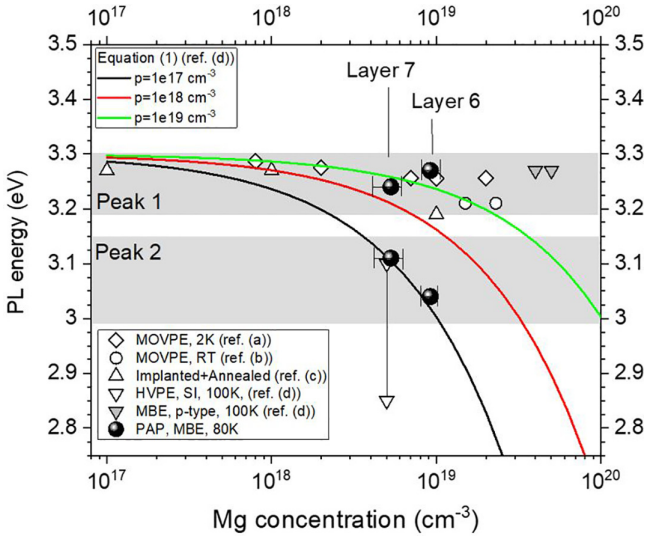

FIG. 5. Correlation of spectral and APT data and comparison with the literature. PL energy of Peaks 1 and 2 (filled circles) as a function of the Mg concentration within the evaporating layer. The data are compared with literature data obtained in samples with different nominal or measured Mg concentration, issued from ref. (a) [27] (open diamonds), ref. (b) [25] (open circles), ref. (c) [42] (open-upward triangles), and ref. (d) [29] (open-downward triangles). The solid lines correspond to the expected maximum of the UVL* luminescence in Mg-doped GaN as a function of the Mg density n_{Mg} for different values of the free carrier density *p*. The grey-horizontal bands indicate the spectral intervals containing the maxima of Peaks 1 and 2.

(ii) Peak 2 may be apparently related either to the emission of the InGaN sections, (waveguide layers at the LD and at the TJ). The InGaN alloy with III-site fraction as found for layers 12, 10, 5, and 2 is expected to luminesce in the same spectral region as Peak 2. However, there are two main arguments against this interpretation: (i) the intensity of Peak 2 rapidly drops to zero just when the evaporation front enters the TJ (Fig. 3, zoom provided in Fig. S4 within the SM [36]) and (ii) according to the SIMS and PAP results, along with the band diagram calculation (Figs. 1 and 3), all InGaN sections contain a high electric field, which is expected to effectively separate the charge carriers generated within them and in their neighborhood. This is especially the case for the TJ, where the field becomes as high as 8 MV/cm. Thus, Peak 2 has rather to be interpreted as due to donor- or band-edge-to-acceptor

diagonal transitions, which are known to occur in highly doped semiconductors [51,52] and are known in the literature on GaN as the UVL* line [29]. A further interpretation, i.e., Peak 2 as a phonon replica of the UVL line [47], is not compatible with the larger intensity of Peak 2 with respect to Peak 1, and with its persistence within layer 6 when Peak 1 vanishes. The intensity increase at d = 700–800 nm can be interpreted as caused by the higher transparency of the specimen apex—a consequence of the evaporation of the lower-bandgap InGaN LD section.

PL at E ∼ 3.1 eV has been reported by different authors. Sheu *et al.* for instance, found it in Mg-doped *n*-type (compensated) GaN [53]. Reshchikov *et al.* have thoroughly characterized the UVL*line [29,54]. This PL component is found in highly doped Mg and can coexist with the UVL due to sample nonuniformity. It characterizes sample regions affected by strong potential fluctuations, either due to the presence of charge impurities or surfaces. The plot in in Fig. 5 reports the energy interval in which these authors have found the UVL* in GaN grown by hydride vapor phase epitaxy (HVPE). In particular, they found that the energy of the peak is strongly dependent on the excitation intensity and, consequently on the free carrier concentration *p*. Weak values of *p* favor diagonal transitions, while large values of *p* tend to screen the potential fluctuations induced by the presence of charged dopants and repristinate vertical transitions at higher energy. The PL maxima are expected to approximately follow the expression [29,55,56]

$$E_{PL} = E_g - E_{Mg} - 2\frac{e^2}{4\pi\varepsilon_s\varepsilon_0}\frac{n_{Mg}^{2/3}}{p^{1/3}}, \tag{1}$$

where $E_g = 3.45$ eV is the GaN bandgap, $E_{Mg} = 0.15$ eV is the acceptor energy above the valence band edge [29], $\varepsilon_s = 8.9$ is the dielectric permittivity of GaN [57], and e is the electron charge. The fraction in Eq. (1) represents the effective amplitude of the potential fluctuations. The trends of the PL energies for different values of p are reported in Fig. 5 and show that the position of the UVL* line is expected to red-shift with increasing doping concentration. The two data point appear as remarkably consistent with the trend for $p = 10^{17}$ cm^{-3}. However, care should be taken before applying the trends of Eq. (1) to the PAP data. Certainly, the effective free carrier density could be as low as 10^{17} cm^{-3}, as transitions could take place in peripheral areas of the sample, close to the surface or at least to the interface with the outer layer damaged by FIB during sample preparation. Furthermore, PL is collected in the PAP under constant impinging laser intensity, but it is known that the effectively absorbed light can vary as the evaporation front gets close to the emitting region [45]. The present data indicate the same trend as Eq. (1), i.e., a red shift of the PL with increasing n_{Mg}. This suggests that the shift from $E_{PL2} = 3.11$ eV to $E_{PL2} = 3.05$ eV could be partly due to the increase in potential fluctuations—in this case the PL signal would originate from both layers 6 and 7. An alternative interpretation is based on the increase of the hydrostatic strain when the evaporation front enters layer 6—in this second case the PL signal would originate from layer 6 only. The strong decrease of the intensity simultaneous to the red shift points rather out to the first interpretation.

Strain-related shifts. It should be mentioned that PL peak shifts in PAP may caused not only by the evaporation front crossing layers of different composition, but also to the effect of the composition of the evaporating layer on the surface field. It is known that in III-N materials the surface field needed to evaporate AlGaN or InGaN requires a higher field than GaN for constant evaporation rate. As surface field generates hydrostatic tensile stress at the apex of the specimen, and uniaxial stress in the shank far from the apex [58,59], crossing InGaN layers would increase the stress and induce a red shift of the PL peaks (notice that typically hydrostatic stress is exerted as a pressure, i.e., a *compressive* stress, in APT, on the contrary, hydrostatic stress is tensile and can reach several GPa [46]). Conversely, entering GaN sections after the evaporation of InGaN would relieve the stress and produce blue shifts. Such shifts are quite clearly visible for Peak 2. The red shift of Peak 2 preceding the intensity increase at the start of the upper waveguide layer 10 can be interpreted as due to the increase in the surface electric field during the evaporation of the InGaN waveguide. The corresponding increase of stress is exerted on the whole specimen, but is higher in the immediate neighborhood of the waveguide itself. Peak 2 then blue shifts at $d \sim 800$ nm because the LD InGaN section is evaporated and the surface field decreases. Its rapid red shift at $d \sim 1300$ nm (layer 6) is related to the increase in Mg concentration, as we argued previously. A new increase in the field and a subsequent new red shift accompany the Peak 2 just during its rapid bleaching, when the evaporation front reaches the TJ. Intriguingly, the energy shifts of Peak 1 and Peak 2 tend to occur in opposite directions. For instance, after the evaporation of the InGaN LD section Peak 2 blue shifts, while Peak 1 red shifts. Again, during the evaporation of layer 6 Peak 1 red shifts, while Peak 2 blue shifts. The shift of Peak 2 can be easily interpreted, as GaN and low-In content InGaN decrease their energy gap for increasing hydrostatic *tensile* stress. The blue shift of the DAP-related Peak 1 is certainly not related to an increase in the tensile hydrostatic stress, as in this case we should expect a red shift [60]. At present, we have no explanation for this behavior. However, we should also be aware that the shifts of Peak 1 are smaller than those affecting Peak 2, and that the broader line shape of Peak 2 could have an effect on the accuracy of the fit of the max of Peak 1.

V. CONCLUSIONS

This paper presented a correlative analysis of the 3D distribution of chemical species and optical emission properties in a thick III-N device structure, containing AlGaN, GaN, and InGaN sections. Besides providing the quantitative assessment of alloy fractions and doping concentrations of Mg and Ge throughout the device, the PAP allows correlating this information with the different components of the GaN subbandgap PL. In particular, it could be demonstrated that the two main overlapping PL peaks, named here Peak 1 (peak energy in the interval $E_{PL1} = 3.19$–3.3 eV) and Peak 2 ($E_{PL2} = 2.98-3.16$ eV) are related to the presence of Mg impurities. Peak 1 is related to vertical DAP or band-to-acceptor transitions (UVL line), while Peak 2 is rather related to diagonal transitions (UVL*). The shift of Peak 2 is also correlated with the variation of Mg concentration within the different sections

of the heterostructure, as reported in previous studies focusing on bulk samples. The main advance that the PAP enabled for the study of this system is the direct correlation between the 3D distribution of Mg in terms of concentration and absence of clustering, and the properties of the sub-bandgap PL, which also contributes to validate the models proposed in the recent past on this specific problem [48]. This study shows that PAP can be applied to the study of point defect luminescence in actual device structures. This not only concerns laser diodes, but potentially all device structures in which defects and/or alloys carry important information via their optical emission. Finally, this study shows that PAP is of potential interest for the study of the microscopic correlation of the optical signatures and chemical/structural properties of defects within a microscopic volume—possibly for the correlative study of the optically active single point defects.

ACKNOWLEDGMENTS

This work is supported by the French Renatech Network, the French National Research Agency (ANR) through the Grants ANR-21-CE50-0016 “Ascese-3D”, and Labex EMC3 “X-PAP” and by National Science Centre, Poland Grant No. 2021/43/D/ST3/03266.

[1] L. F. Zagonel, Nanometer scale spectral imaging of quantum emitters in nanowires and its correlation to their atomically resolved structure, Nano Lett. **11**, 568 (2011).

[2] D. A. M. De Winter, M. N. Lebbink, D. F. W. De Vries, J. A. Post, and M. R. Drury, FIB-SEM cathodoluminescence tomography: Practical and theoretical considerations, J. Microscopy **243**, 315 (2011).

[3] W. Hahn, Evidence of nanoscale Anderson localization induced by intrinsic compositional disorder in InGaN/GaN quantum wells by scanning tunneling luminescence spectroscopy, Phys. Rev. B **98**, 045305 (2018).

[4] J. Nelayah, Mapping surface plasmons on a single metallic nanoparticle, Nat. Phys. **3**, 348 (2007).

[5] E. Di Russo, Super-resolution optical spectroscopy of nanoscale emitters within a photonic atom probe, Nano Lett. **20**, 8733 (2020).

[6] J. Houard, A photonic atom probe coupling 3D atomic scale analysis with *in situ* photoluminescence spectroscopy, Rev. Sci. Instruments **91**, 083704 (2020).

[7] X. Wang and A. Yoshikawa, Molecular beam epitaxy growth of GaN, AlN and InN, Prog. Crystal Growth Charact. Mater. **48-49**, 42 (2004).

[8] I. M. Watson, Metal organic vapour phase epitaxy of AlN, GaN, InN and their alloys: A key chemical technology for advanced device applications, Coord. Chem. Rev. **257**, 2120 (2013).

[9] A. Cremades, L. Görgens, O. Ambacher, M. Stutzmann, and F. Scholz, Structural and optical properties of Si-doped GaN, Phys. Rev. B **61**, 2812 (2000).

[10] R. Kirste, Ge doped GaN with controllable high carrier concentration for plasmonic applications, Appl. Phys. Lett. **103**, 242107 (2013).

[11] A. Ajay, Ge doping of GaN beyond the Mott transition, J. Phys. D: Appl. Phys. **49**, 445301 (2016).

[12] P. Bogusławski and J. Bernholc, Doping properties of C, Si, and Ge impurities in GaN and AlN, Phys. Rev. B **56**, 9496 (1997).

[13] L. Konczewicz, Electrical transport properties of highly doped N-type GaN materials, Semicond. Sci. Technol. **37**, 055012 (2022).

[14] E. D. Russo, Multi-microscopy nanoscale characterization of the doping profile in a hybrid Mg/Ge-doped tunnel junction, Nanotechnology **31**, 465706 (2020).

[15] H. Amano, M. Kitoh, K. Hiramatsu, and I. Akasaki, Growth and luminescence properties of Mg-doped GaN prepared by MOVPE, J. Electrochem. Soc. **137**, 1639 (1990).

[16] C. Skierbiszewski, Nitride-based laser diodes grown by plasma-assisted molecular beam epitaxy, J. Phys. D: Appl. Phys. **47**, 073001 (2014).

[17] M. J. Grundmann and U. K. Mishra, Multi-color light emitting diode using polarization-induced tunnel junctions, Phys. Status Solid. C **4**, 2830 (2007).

[18] H. Turski, S. Bharadwaj, H. (Grace) Xing, and D. Jena, Polarization control in nitride quantum well light emitters enabled by bottom tunnel-junctions, J. Appl. Phys. **125**, 203104 (2019).

[19] H. Turski, Nitride LEDs and lasers with buried tunnel junctions, ECS J. Solid State Sci. Technol. **9**, 015018 (2019).

[20] S. E. Bennett, Atom probe tomography and transmission electron microscopy of a Mg-doped AlGaN/GaN superlattice, Ultramicroscopy **111**, 207 (2011).

[21] L. Amichi, Three-dimensional measurement of Mg dopant distribution and electrical activity in GaN by correlative atom probe tomography and off-axis electron holography, J. Appl. Phys. **127**, 065702 (2020).

[22] A. S. Chang, Selective area regrowth produces nonuniform Mg doping profiles in nonplanar GaN p–n junctions, ACS Appl. Electron. Mater. **3**, 704 (2021).

[23] M. Leroux, Pyramidal defects in highly Mg-doped GaN: Atomic structure and influence on optoelectronic properties, Eur. Phys. J. Appl. Phys. **27**, 259 (2004).

[24] M. A. Reshchikov, G.-C. Yi, and B. W. Wessels, Behavior of 2.8- and 3.2-eV photoluminescence bands in Mg-doped GaN at different temperatures and excitation densities, Phys. Rev. B **59**, 13176 (1999).

[25] U. Kaufmann, Origin of defect-related photoluminescence bands in doped and nominally undoped GaN, Phys. Rev. B **59**, 5561 (1999).

[26] S. Strauf, Analysis of time-resolved donor–acceptor-pair recombination in MBE and MOVPE grown GaN: Mg, Phys. Status Solid. B **228**, 379 (2001).

[27] G. Callsen, Optical signature of Mg-doped GaN: Transfer processes, Phys. Rev. B **86**, 075207 (2012).

[28] B. Monemar, Luminescence of acceptors in Mg-doped GaN, Jpn. J. Appl. Phys. **52**, 08JJ03 (2013).

[29] M. A. Reshchikov, P. Ghimire, and D. O. Demchenko, Magnesium acceptor in gallium nitride. I. Photoluminescence from Mg-doped GaN, Phys. Rev. B **97**, 205204 (2018).

[30] E. Kioupakis, P. Rinke, and C. G. V. de Walle, Determination of internal loss in nitride lasers from first principles, Appl. Phys. Express **3**, 082101 (2010).
[31] Y.-R. Wu, C. Chiu, C.-Y. Chang, P. Yu, and H.-C. Kuo, Size-dependent strain relaxation and optical characteristics of InGaN/GaN nanorod LEDs, IEEE J. Sel. Top. Quantum Electron. **15**, 1226 (2009).
[32] M. Ilegems and R. Dingle, Luminescence of Be- and Mg-doped GaN, J. Appl. Phys. **44**, 4234 (1973).
[33] D. Blavette, A. Bostel, J. M. Sarrau, B. Deconihout, and A. Menand, An atom probe for three-dimensional tomography, Nature (London) **363**, 432 (1993).
[34] B. Gault, Design of a femtosecond laser assisted tomographic atom probe, Rev. Sci. Instrum. **77**, 043705 (2006).
[35] G. D. Costa, H. Wang, S. Duguay, A. Bostel, D. Blavette, and B. Deconihout, Advance in multi-hit detection and quantization in atom probe tomography, Rev. Sci. Instrum. **83**, 123709 (2012).
[36] See Supplemental Material at http://link.aps.org/supplemental/10.1103/PhysRevMaterials.8.074603 concerning mass spectra analysis, characterization of the Ge doping and details on the analysis of the PL spectra is provided as a separate pdf file,
[37] F. Meisenkothen, D. V. Samarov, I. Kalish, and E. B. Steel, Exploring the accuracy of isotopic analyses in atom probe mass spectrometry, Ultramicroscopy **216**, p. 113018 (2020).
[38] F. Vurpillot, Chapter Seven - Three-dimensional reconstruction in atom Pprobe tomography: Basics and advanced approaches, in *Atom Probe Tomography* (Academic Press, New York, 2016), pp. 183–249.
[39] E. Di Russo, Compositional accuracy in atom probe tomography analyses performed on III-N light emitting diodes, J. Appl. Phys. **126**, 124307 (2019).
[40] A. Diagne, Field-dependent abundances of hydride molecular ions in atom probe tomography of III-N semiconductors, J. Microsc. **293**, 153 (2024).
[41] L. Amichi, Correlative investigation of Mg doping in GaN layers grown at different temperatures by atom probe tomography and off-axis electron holography, Nanotechnology **31**, 045702 (2019).
[42] A. Kumar, Influence of implanted Mg concentration on defects and Mg distribution in GaN, J. Appl. Phys. **128**, 065701 (2020).
[43] W. S. M. Werner, K. Glantschnig, and C. Ambrosch-Draxl, Optical constants and inelastic electron-scattering data for 17 elemental metals, J. Phys. Chem. Ref. Data **38**, 1013 (2009).
[44] J. W. Cleary, Platinum germanides for mid- and long-wave infrared plasmonics, Opt. Express **23**, 3316 (2015).
[45] E. M. Weikum, Influence of dynamic morphological modifications of atom probe specimens on the intensity of their photoluminescence spectra, J. Opt. Soc. Am. B **40**, 1633 (2023).
[46] P. Dalapati, *In situ* spectroscopic study of the optomechanical properties of evaporating field ion emitters, Phys. Rev. Appl. **15**, 024014 (2021).
[47] B. Monemar, Evidence for two Mg related acceptors in GaN, Phys. Rev. Lett. **102**, 235501 (2009).
[48] M. A. Reshchikov, Measurement and analysis of photoluminescence in GaN, J. Appl. Phys. **129**, 121101 (2021).
[49] A. R. Persson, A. Papamichail, V. Darakchieva, and P. O. Å. Persson, Mg segregation at inclined facets of pyramidal inversion domains in GaN:Mg, Sci. Rep. **12**, 1 (2022).
[50] A. Kumar, Atomic-scale quantitative analysis of implanted Mg in annealed GaN layers on free-standing GaN substrates, J. Appl. Phys. **126**, 235704 (2019).
[51] J. Qiu, J. M. DePuydt, H. Cheng, and M. A. Haase, Heavily doped *p*-ZnSe:N grown by molecular beam epitaxy, Appl. Phys. Lett. **59**, 2992 (1991).
[52] H. P. Gislason, B. H. Yang, and M. Linnarsson, Shifting photoluminescence bands in high-resistivity Li-compensated GaAs, Phys. Rev. B **47**, 9418 (1993).
[53] J. K. Sheu, Photoluminescence spectroscopy of Mg-doped GaN, J. Appl. Phys. **84**, 4590 (1998).
[54] M. A. Reshchikov, Giant shifts of photoluminescence bands in GaN, J. Appl. Phys. **127**, 055701 (2020).
[55] B. I. Shklovskii and A. L. Efros, The structure of the impurity band for lightly doped semiconductors, in *Electronic Properties of Doped Semiconductors*, edited by B. I. Shklovskii and A. L. Efros (Springer, Berlin, 1984), pp. 52–73.
[56] A. P. Levanyuk and V. V. Osipov, Edge luminescence of direct-gap semiconductors, Sov. Phys. Usp. **24**, 187 (1981).
[57] S. Yu. Davydov, Estimates of the spontaneous polarization and permittivities of AlN, GaN, InN, and SiC crystals, Phys. Solid State **51**, 1231 (2009).
[58] P. Perlin, I. Gorczyca, N. E. Christensen, I. Grzegory, H. Teisseyre, and T. Suski, Pressure studies of gallium nitride: Crystal growth and fundamental electronic properties, Phys. Rev. B **45**, 13307 (1992).
[59] S. Kim, I. P. Herman, J. A. Tuchman, K. Doverspike, L. B. Rowland, and D. K. Gaskill, Photoluminescence from wurtzite GaN under hydrostatic pressure, Appl. Phys. Lett. **67**, 380 (1995).
[60] H. Teisseyre, Different character of the donor-acceptor pair-related 3.27 eV band and blue photoluminescence in Mg-doped GaN. Hydrostatic pressure studies, Phys. Rev. B **62**, 10151 (2000).